

Spectrophotometric Observations of Blue Compact Dwarf Galaxies: Mrk 370

Luz M. Cairós

luzma@uni-sw.gwdg.de

Universitäts-Sternwarte Göttingen, Geismarlandstr. 11, 37083, Göttingen, Germany. Instituto de Astrofísica de Canarias, E-38200 La Laguna, Tenerife, Canary Islands, Spain. Departamento de Astronomía, Universidad de Chile, Casilla 36-D, Santiago, Chile

Nicola Caon

ncaon@ll.iac.es

Instituto de Astrofísica de Canarias, E-38200 La Laguna, Tenerife, Canary Islands, Spain

Begoña García Lorenzo

bgarcia@ing.iac.es

Isaac Newton Group of Telescopes (ING), E-38780 Santa Cruz de La Palma, La Palma, Canary Islands, Spain

José M. Vilchez

jvm@iaa.es

Instituto de Astrofísica de Andalucía, CSIC, Apdo. 3004, 18080 Granada, Spain

Casiana Muñoz-Tuñón

cmt@ll.iac.es

Instituto de Astrofísica de Canarias, E-38200 La Laguna, Tenerife, Canary Islands, Spain

ABSTRACT

We present results from a detailed spectrophotometric analysis of the blue compact dwarf galaxy (BCD) Mrk 370, based on deep *UBVRI* broad-band and H α narrow-band observations, and long-slit and two-dimensional spectroscopy of its brightest knots.

The spectroscopic data are used to derive the internal extinction, and to compute metallicities, electronic density and temperature in the knots. By subtracting the contribution of the underlying older stellar population, modeled by an exponential function, removing the contribution from emission lines, and correcting for extinction, we can measure the true colors of the young star-forming knots. We show that the colors obtained this way differ significantly from those derived without the above corrections, and lead to different estimates of the ages and star-forming history of the knots. Using predictions of evolutionary synthesis models, we estimate the ages of both the starburst regions and the underlying stellar component. We found that we can reproduce the colors of all the knots with an instantaneous burst of star formation and the Salpeter initial mass function (IMF) with an upper mass limit of 100 M $_{\odot}$. The resulting ages range between 3 and 6 Myrs. The colors of the low surface brightness component are consistent with ages larger than 5 Gyr. The kinematic results suggest ordered motion around the major axis of the galaxy.

1. Introduction

Blue Compact Dwarf galaxies (BCD) are low-luminosity ($M_B \geq -18$ mag), compact (starburst diameter ≤ 1 kpc) objects, which have optical spectra similar to those presented by H II regions in spiral galaxies (Sargent & Searle 1970; Thuan & Martin 1981). They are metal deficient galaxies — the metallicities of their ionized gas ranging between $Z_\odot/50$ and $Z_\odot/2$ — that form stars at high rates, able to exhaust their available gas content in a time much smaller than the age of the Universe. This fact implies that either these galaxies are young systems, experiencing their first burst of star formation, or that star formation occurs in short bursts separated by long quiescent periods (Sargent & Searle 1970). Nowadays, the latter explanation is the more widely accepted, at least for the majority of BCDs (Thuan 1991).

In the recent years BCDs have attracted a great deal of interest, and have become key objects for understanding fundamental astrophysical problems. Much effort has been devoted to the study of these galaxies, driven by the following fundamental questions: 1) what is the mechanism that triggers the starburst activity and is there a unique one in all BCD subtypes? 2) what are the properties of the underlying stellar population (age, metallicity, dynamical status)? Answering the above questions would allow to form a general view of dwarf galaxy formation and evolution, and in particular to test those evolutionary scenarios linking the different classes of dwarf galaxies, namely, dwarf irregulars (dIs), dwarf ellipticals (dEs) and BCDs (Thuan 1985; Davies & Phillipps 1988; Papaderos et al. 1996b; Marlowe et al. 1997; Marlowe, Meurer, & Heckman 1999), or the different morphological classes of BCDs (Noeske et al. 2000). However, most of the work carried out so far has focused on a statistical analysis of BCD samples by means of surface photometry (Papaderos et al. 1996a; Telles 1995; Doublier et al. 1997; Doublier, Caulet, & Comte 1999; Östlin 1998), and has rather demonstrated the complexity of the topic than given firm answers.

Prompted by this lack of conclusive results, we started an extensive study of a large sample of BCDs. The first step was the analysis of broad-band observations in B , V , R and I for a sample of 28 BCDs. In Cairós et al. (2001a, hereafter

Paper I) we presented deep contour maps in the B band, and surface brightness and color profiles, which were used to examine and discuss their morphology and structure. In Cairós et al. (2001b, hereafter Paper II) we enlarged the dataset by including U and $H\alpha$ observations; we provided integrated photometry of the galaxies and produced an atlas of detailed color and $H\alpha$ maps. The quality of the data allowed us to identify the different star-forming regions, and discriminate them from the regions where the star formation has already ceased.

One of our main conclusions was that optical broad-band photometry alone does not allow to disentangle the distinct stellar components in BCDs and derive their evolutionary status. The measured broad-band colors are strongly affected by interstellar reddening and gaseous emission; besides, we need to separate the light coming from young stars from the emission of those born in previous star-formation episodes — a methodological aspect often overlooked. Spectroscopic information is required in order to correct for interstellar reddening and emission line contamination, and U -band and $H\alpha$ measurements are fundamental, since they are much more sensitive to the star-formation properties. Nevertheless, such kind of analysis is scarce in the literature, mainly because it requires a lot of observing time. In particular, not enough effort has been devoted so far to the characterization of the stellar population hosting the actual burst, indeed a challenging task.

For these reasons, we decided to perform a more detailed study of a number of individual galaxies, based on a new strategy that combines broad- and narrow-band photometry with long-slit and 2-D spectroscopy. The objects were selected among those presented in Papers I and II, so as to form a sample including the different subtypes of objects classified as BCDs — a not so well defined class which spans a wide range of luminosities, metallicities and morphologies (Kunth & Östlin 2000; Cairós 2000; Cairós et al. 2001b).

This paper is the first in a series which present the results obtained from the use of this technique to analyze the selected galaxies. Here we describe the technique and its application to the galaxy Mrk 370, a luminous BCD, with $M_B = -17.20$ (Paper II), located at a distance of 12.9 Mpc

(Thuan & Martin 1981)¹.

We have chosen this galaxy in order to study a prototype of the group of BCDs populating the higher luminosity and metallicity range within the most common BCD morphological subclass, the iE type (Loose & Thuan 1986, hereafter LT86). This type is characterized by an underlying, low brightness elliptical component which hosts numerous star-forming regions.

In Mrk 370, the brighter knots of star-formation are located in the inner part of the galaxy, from where smaller star-forming knots emerge and form a structure resembling spiral arms (see Papers I and II). The choice of Mrk 370 rests also on the fact that the comparison of the properties of its many individual starburst knots provides valuable information on the mechanisms that trigger the star formation, allowing to study how it propagates within the galaxy, and is a possible test of the stochastic self-propagating star formation mechanism (Gerola, Seiden, & Schulman 1980), which has been suggested to explain how the star-formation process in dwarfs is maintained (Coziol 1996).

In addition, Mrk 370 may be seen as a prototype of the BCDs classified as multiple nucleus starburst galaxies. The presence of two central star-forming knots led Mazzarella & Boroson (1993) to label this galaxy as a "double nucleus" BCD, prompting further suggestions of its merger origin. As we will show in this work, the kinematic and spectrophotometric results obtained cast serious doubts on the merger scenario.

A complete collection of color and H α maps of this galaxy can be found at the following Web page: <http://www.iac.es/proyecto/GEFE/BCDs>. The basic data of Mrk 370 are shown in Table 1.

2. Observations and Data Reduction

2.1. Long-slit spectra

Long-slit spectroscopy of Mrk 370 was obtained in September 1998, with the Isaac Newton Tele-

¹For consistency with Papers I and II, we use here the distance from Thuan & Martin (1981), which is based on the radial velocity with respect to the Local Group and $H_0 = 75 \text{ km sec}^{-1} \text{ Mpc}^{-1}$; applying the correction for LG infall into Virgo would give $D = 10.9 \text{ Mpc}$, and total luminosities, absolute magnitudes and sizes would change accordingly.

scope (INT) at the Observatorio del Roque de Los Muchachos (ORM, La Palma). The data were taken using the Intermediate Dispersion Spectrograph (IDS), equipped with a CCD. A slit 3'8 long and 1''2 wide was used. The position angle of the slit was set to 125°, so as to pass through the two brightest central knots. The spectral sampling was 1.85 Å per pixel, the wavelength range 3600–7300 Å, and the spectral resolution $\sim 5.5 \text{ Å}$ (FWHM); the spatial sampling was 0.39 arcsec per pixel. The seeing was about 1''.5. The log of the observation is shown in Table 2.

Data reduction was performed using **IRAF** standard tasks: after subtracting the bias and flat-fielding the spectra, they were calibrated in wavelength. The sky spectrum was derived by averaging the signal in two windows 30–40 pixel wide outside the region where the object is still detectable, and subtracted out. The spectra were then corrected for atmospheric extinction and calibrated in flux by means of observations of spectrophotometric standards.

2.2. Two-dimensional spectroscopy

The 4.2m William Herschel Telescope (WHT, at the ORM, La Palma), equipped with the fiber system INTEGRAL (Arribas et al. 1998) and the WYFFOS spectrograph (Bingham et al. 1994), was used to observe the central region of Mrk 370.

INTEGRAL currently has three fiber bundles with different spatial configurations on the focal plane. These three bundles can be interchanged during the observations depending on the scientific program or the seeing conditions. On the focal plane, the fibers of each bundle are arranged in two groups: one forms a rectangle which maps the object, the other forms an outer ring which samples the sky-background. Mrk 370 observations were done with the standard bundle 2 (hereafter SB2). It consists of 219 fibers, each 0''.9 in diameter; the central rectangle is formed by 189 fibers covering an area of 16'' \times 12''.3, while the other 30 fibers are evenly spaced on a ring 90'' in diameter. Figure 1 shows the actual distribution of those fibers in the focal plane. At the entrance of the WYFFOS spectrograph, the fibers are aligned so as to form a pseudo-slit.

We observed Mrk 370 on August 22 1999, with a seeing of $\sim 1''.3$. The spectrograph was equipped

with a grating of 600 groove/mm, and a Tek6 CCD array of 1124x1124 24-micron pixels. The spectral range coverage was 4400 – 7150 Å, with a spectral resolution of about 6 Å; it includes the H β , [O III], H α , [N II], and [S II] emission lines (see Appendix A).

Data reduction was performed within the IRAF environment, and includes bias and scattered light subtraction, fiber extraction, fiber throughput correction, wavelength calibration, rejection of cosmic ray events, and correction from differential atmospheric refraction effects (for details on reduction of fiber data see e.g. García-Lorenzo, Mediavilla, & Arribas 1999, and references therein).

In Appendix A we present the nuclear spectrum of Mrk 370 in the full wavelength range observed with the fiber system. We also show the individual spectra corresponding to each of the 189 observed positions (fibers) in a selected spectral interval which includes the most important emission lines.

2.3. H α imaging

Narrow-band images centered on the H α line and on the adjacent continuum were taken in 1997 December at the 2.2-m telescope of the German-Spanish Astronomical Observatory on Calar Alto (Almería, Spain). The instrumentation consisted of the *Calar Alto Faint Object Spectrograph*, CAFOS, and a 2048 × 2048 SiTe CCD chip. With a pixel size of 0.53 arcsec, it provides a field 16 arcmin wide; however, due to the physical size of the available filters, only the central round area of about 11 arcmin is free from vignetting. The average seeing was 1.5 arcsec.

The image reduction was carried out using IRAF. Each image was corrected for bias, using an average bias frame, and was flattened by dividing by a mean twilight flatfield image. The frames were then registered (for each filter we took a set of dithered exposures) and combined to obtain the final frame, with cosmic ray events removed and bad pixels cleaned out. The average sky level was estimated by computing the mean value within several boxes surrounding the object, and subtracted out as a constant. Flux calibration was done through the observation of spectrophotometric stars from the lists in Oke (1990).

The complete log of the observations is shown

in Table 2.

2.4. Broadband Imaging

UBVRI imaging of Mrk 370 was carried out in October 1998 at the 1-m Jacobus Kapteyn Telescope, JKT (ORM, La Palma). We collected CCD images at the f/15 Cassegrain focus, using a Tek 1024 × 1024 pixel chip, yielding a pixel size of 0.33 arcsec and a field of view of 5.6 × 5.6 arcmin. The average seeing was 1''.5.

A log of the observations is given in Table 2. The image processing was performed using standard procedures available in IRAF. Flux calibration was done through the observation of photometric stars from Landolt (1992) throughout the night.

3. Spectroscopic Analysis

3.1. Long-slit spectroscopy

The position of the slit we used is shown in Figure 2, overplotted on a contour map of the continuum-subtracted H α image. (The meaning of the labels is explained in Section 4). The spatial run of the intensity of the brightest emission lines (H α , H β , [O III]) has been used as a base for defining the regions from where the one-dimensional spectra of each knot were extracted by integrating the signal within them. Two distinct starburst regions have been identified, marked A and B in Figure 2.

Figure 3 shows the summed spectra of the two knots, and the spectrum integrated over the whole galaxy (which we shall refer to as S). The spectrum of region A shows a high continuum level. Absorption wings are resolved in H β and H γ , H δ being visible in absorption only. The Balmer discontinuity, together with these absorption features, can be interpreted as the product of a substantial population of older stars, with ages considerably larger than 10 million years. Region B shows an almost flat spectrum, characteristic of a dominant OB population, with no evident absorption features. The integrated spectrum, S, is similar to that of region A.

Fluxes and equivalent widths of the emission lines were measured using the gaussian profile fitting option in the iraf task SPLOT (a direct integration of the flux inside each line gave very simi-

lar results). It is known that these measurements are an underestimate of the real flux of the Balmer lines, because of the underlying absorption component. In the present spectra we could not deblend the two components. To correct for the underlying stellar absorption, some authors (McCall, Rybski & Shields 1985; Skillman & Kennicutt 1993) adopt a constant equivalent width ($1.5 - 2 \text{ \AA}$) for all the hydrogen absorption lines. However, the actual value of their equivalent width is uncertain and depends on the age of the star formation burst (Díaz 1988; Cananzi, Augarde, & Lequeux 1993; Olofsson 1995). Thus we preferred to leave it as a free parameter, which was determined as follows.

We assume that the equivalent width, W_{abs} , of the absorption line is the same for all the Balmer lines, but can vary from knot to knot. We then start with an initial guess for W_{abs} , correct the measured fluxes, and determine the extinction coefficient at $\lambda = 4861 \text{ \AA}$, $C(\text{H}\beta)$, and its uncertainty, $\Delta C(\text{H}\beta)$, through a fit to the Balmer decrement, given by the equation:

$$\frac{F(\lambda)}{F(\text{H}\beta)} = \frac{I(\lambda)}{I(\text{H}\beta)} \times 10^{C(\text{H}\beta) \times f(\lambda)} \quad (1)$$

where $\frac{F(\lambda)}{F(\text{H}\beta)}$ is the line flux corrected for absorption and normalized to $\text{H}\beta$; $\frac{I(\lambda)}{I(\text{H}\beta)}$ is the theoretical value for case B recombination, from Brocklehurst (1971), and $f(\lambda)$ is the reddening curve normalized to $\text{H}\beta$ which we took from Whitford (1958).

We then search, for each knot, the value of W_{abs} that provides the best match — that is, the lowest $\Delta C(\text{H}\beta)$ — between the corrected and the theoretical line ratios.

Reddening-corrected intensity ratios and equivalent widths are quoted in Table 3.

The [O III] $\lambda 4363$ line could not be detected in the spectra, so the oxygen abundance for the different regions of Mrk 370 was derived using the empirical $12 + \log \text{O/H}$ vs R_{23} relation, first derived by Pagel et al. (1979). We have used the R_{23} calibration according to McGaugh (1991). The ratio [N II]/[O II] was used to break the degeneracy in the calibration in order to select either the upper or the lower branch (McGaugh 1991). Since the values of [N II]/[O II] for the three spectra analyzed are always above the 0.1 threshold ($\log \lambda 6584/\lambda 3727 = -0.59, -0.81, -0.75$ for re-

gions A, B and S), the upper branch of the calibration has been used for the determination of the abundance. We have derived the following values: $12 + \log \text{O/H} = 8.7, 8.6$ and 8.7 for the spectra of regions A, B and S respectively, for which the corresponding values for the logarithm of electron density are $2.07, 2.2$ and 2.3 .

The average value for the nitrogen to oxygen ratio is $\log N/O = -1.1$. The derived average oxygen abundance is approximately $Z_{\odot}/2$. The abundances are equal for regions A and B, within the uncertainties.

3.2. Two-dimensional spectroscopy

Two-dimensional spectroscopy with optical fibers allows to collect simultaneously the spectra of many different regions of an extended object, combining photometry and spectroscopy in the same dataset.

From the individual measurements (line fluxes and ratios, continuum level, radial velocity, etc.) obtained at each fiber, we can build 2-D maps by using a two-dimensional interpolation technique, such as the Renka & Cline algorithm (implemented in the E01SAF and E01SBF routines in the NAG Fortran Library). This requires a precise knowledge of the exact location of each fiber, which is determined by a metrology machine. In this way we built up images of 95×95 pixels with a scale $\sim 0''.2 \text{ pixel}^{-1}$. While the spatial sampling (that is, the fiber diameter) of INTEGRAL (STD2) is 0.9 arcsec , the centroid of any peak in our maps can be measured with an accuracy of around 0.2 arcsec (that is $1/5$ of the fiber diameter; see for instance Mediavilla et al. 1998)

3.2.1. Continuum and Line-Intensity Maps

Because of non-photometric conditions during INTEGRAL observations, we could not flux-calibrate directly our spectra. The flux calibration was done by using the long-slit data as a reference. We integrated the signal in our 2-D spectra within two regions matching regions A and B in the long-slit spectra. Comparing the fluxes of different lines, we could compute the conversion factor with an accuracy of about 20%. This is the error associated to the fluxes derived from INTEGRAL data using this calibration.

Figure 4(a) shows a continuum map (within

a spectral region where no emission lines are present) of Mrk 370 from INTEGRAL spectra. We also present in Figure 4(b) a V band image of the galaxy, in order to evidence the excellent agreement between the continuum map and the broad-band images.

The INTEGRAL data show that the position of the peak in the continuum maps does not depend on what spectral range was used to build them. Therefore, we can safely define this point as the "optical nucleus" of the galaxy, and we set it as the origin of the coordinate system in all our spectral maps.

By fitting a single-gaussian to each emission line in our spectra, we have obtained emission line flux maps. Figure 4 (c) shows the $H\alpha$ emission map. We also fitted an absorption component to Balmer lines in those spatial positions where the absorption wings were clear. For comparison, an $H\alpha$ narrow band filter image of Mrk 370 is displayed in Figure 4 (d). The area covered by INTEGRAL includes four of the many star-forming knots present in the galaxy. The optical nucleus does not coincide with any of them.

Figure 4 (e) is the map of the $[O\ III]/H\beta$ ratio, which is commonly used as an indicator of the excitation. The morphology of the $[O\ III]/H\beta$ map is similar to the emission lines intensity maps. The regions with the highest ionization coincide with the knot peaks, and the level of excitation is normal for star-forming regions. Figure 4 (f) is the map of the extinction coefficient $C(H\beta)$ computed from the observed $H\alpha/H\beta$ ratio.

The peaks in the extinction coefficient map are close to, but not coincident with, the peaks of the $H\alpha$ knots. The average offset for the four knots in our observed area is 0.26 ± 0.11 arcsec. While this displacement is small — in fact, it is at our detection limit —, it may suggest a real spatial shift between the center of the HII regions and the *holes* in the $C(H\alpha)$ distribution. A similar case has been reported before by Maíz-Apellaniz et al. (1998) for the starburst knots of the galaxy NGC 4214. They find the dust to be concentrated at the boundaries of the ionized regions. The explanation that they propose is that stellar winds have contributed to diffuse the dust into the inter-cluster medium.

3.2.2. Kinematical Pattern

The kinematic analysis is limited to the emission features, as absorption lines are too weak to be of some utility.

Individual Radial Velocities

Radial velocities were obtained by fitting a single gaussian to each emission line present in our spectra. Although the spectral resolution of the Integral Field Spectroscopy is ~ 275 km/s, the centroid of the emission features could be measured with an accuracy of ± 10 km/s, as indicated by the scatter among the radial velocities obtained from different lines. The final radial velocities of the ionized gas were obtained by averaging the results derived from individual emission lines. We compared the results for the two different individual exposures of Mrk 370. The mean difference among the individual values was 0 ± 12 km/s. Therefore, by adding the error on the wavelength calibration (~ 7 km/s), we estimate that the final uncertainties on the velocity measurements are $\lesssim 20$ km/s.

The Mean Ionized Gas Velocity Field

Figure 5 shows that the velocity field appears to be regular and similar to that of a rotating disk. The west region is receding, the east part is approaching. In order to determine the location of the kinematic center (K hereafter), we computed the "differential" of the velocity field, averaging the absolute differences between one point and its nearest neighbors. This procedure emphasizes regions in which the velocity is changing rapidly. The position derived in this way is placed $\sim 2''4$ SE ($-2''36, 0''37$) of the optical nucleus. K is located between regions A and B, in an apparently non-significant location in the galaxy, and has a velocity value of 766 ± 20 km/s, consistent with the systemic velocity of the galaxy, 783 ± 16 km/s, reported by Falco et al. (2000).

K is nearly coinciding with the geometrical center of the external isophotes, obtained from our broad band images. This fact might suggest that the star-forming knots in the central region of Mrk 370 could share the same velocity field of the main body.

Velocity Field Parameters

To quantify the relevant parameters of the ionized gas velocity field, we adopted a simple kine-

matic model (Mihalas & Binney 1981):

$$V_r(R, \theta) = V_{\text{sys}} + Z(R) \cos i + \Omega(R) \cos[\theta - \delta(R)] \sin i \quad (2)$$

where V_{sys} is the systemic velocity, $\Omega(R)$ is the strength of the velocity field projection onto the galactic plane, and $\delta(R)$ is the PA of the major kinematic axis. R and θ are the galactocentric polar coordinates in the plane of the galaxy.

We fit this model to the data, keeping fixed the position of the center at K, and assuming an initial estimate of the position angle of the kinematical major axis $\delta_0 \sim 90^\circ$, and an inclination of the galaxy $i \sim 40^\circ$ (Nordgren et al. 1995). The results do not depend on δ_0 , and are rather insensitive to reasonable changes in i . In Figure 6 we present the dependence on galactocentric distance of the parameters resulting from the fit. The systemic velocity we derived is 761 km/s, with an internal error of ± 2 km/s.

4. Photometric Analysis

4.1. H α photometry of the starburst knots

The left panel of Figure 7 shows a grey-scale H α image of Mrk 370. The galaxy reveals a complex structure consisting of several resolved knots located atop an extended low surface brightness (LSB) component having regular appearance (see the R band map in Figure 7, right panel) and substantially redder colors (Paper I and Paper II).

In the central part of the galaxy are two large star-forming regions (labeled 11 and 12 in Figure 2), ≈ 7 arcsec (450 pc) apart, which appear to be connected by a faint bridge-like structure; these two star-forming regions have been previously cataloged as "double nucleus" by Mazzarella & Boroson (1993). Smaller star-forming knots extend out in the north-east and south-west directions, to approximately 40 arcsec (2.5 kpc) from the optical center (i.e., the center of the outer isophotes). The star-formation activity is concentrated along this direction, with the exception of region 11).

We have used the FOCAS package to identify and analyze the different knots in the continuum-subtracted H α images. The FOCAS task looks for local maxima and minima in the ADU counts of each pixel in the image. We have adopted the criteria that, for a knot to be detected, its area must be larger than 12 pixels (corresponding to

an equivalent diameter of 2 arcsec or 125 pc), to ensure that the diameter of the knot is larger than the PSF, and the counts of each of its pixels must be higher than 3 times the standard deviation of the sky background. Using these criteria, a total of 16 knots were detected; they are labeled in Figure 2.²

Data on the H α flux, luminosity, number of ionizing photons, ionized hydrogen mass and equivalent width of each knot were calculated; these results are presented in Table 4. The number of ionizing photons and the ionized hydrogen mass were calculated following Kennicutt (1988). The electron temperature and density needed to calculate the mass of the hydrogen ionized gas and the number of ionizing photons were obtained from the long-slit spectra.

The resulting parameters have been corrected for interstellar extinction and for the contribution of the [N II] lines. For the Knots 11 and 12, we used the spectroscopic parameters derived for the subregions B and A (see Figure 2). We used the bi-dimensional data to correct knots inside the INTEGRAL field. For those knots outside the region covered by our 2-D spectra, the above corrections have been applied by using averaged values derived from the central region.

The luminosity of the brightest knots (11 and 12) are comparable to those of individual giant H II regions (typically 10^{39} – 10^{40} erg sec $^{-1}$; Kennicutt 1991). The range in luminosities is similar to that found for the H II regions cataloged in the Magellanic Irregular NGC 4449 (Fuentes-Masip et al. 2000).

The equivalent width $W(\text{H}\alpha)$ was computed as:

$$W(\text{H}\alpha) = C_{\text{H}\alpha} / C_{\text{cont}} \times \Delta W_{\text{H}\alpha} \quad (3)$$

where $C_{\text{H}\alpha}$ is the total number of net counts of the knot, C_{cont} is the corresponding total number of counts in the rescaled continuum image, and $\Delta W_{\text{H}\alpha}$ is the width of the H α filter transmission curve.

The H α equivalent width has been corrected for the contribution of the underlying stellar emission to the continuum level; it means that C_{cont} are the total counts measured in the continuum band

²The Integral continuum maps show another fainter knot, not detected by Focas as it does not satisfy these criteria.

after subtracting the counts due to the emission of the older stars. In order to estimate this latter contribution, we assumed that the underlying population can be described by an exponential model (this procedure is explained in the next section). As the exposures in the continuum narrow-band filter were not deep enough to derive the properties of the underlying disk, the structural parameters derived in R band have been used. The continuum flux map through the $H\alpha$ filter has been derived from the R frame after the latter has been rescaled so as to match the continuum in the former. We followed the same procedure, based on field stars, commonly employed to match $H\alpha$ and its adjacent continuum (see Paper II for a description of this technique).

In Table 4 we show the values of $W(H\alpha)$ of the different star-forming regions in Mrk 370; we have listed the values before and after applying the correction for the contribution of the older stars, to provide a direct estimation of the importance of such contribution. We found the difference to be significant in most cases.

4.2. Broad-band Photometry

4.2.1. The Starburst

The young starburst regions have been isolated in each broad-band filter image. Using FOCAS, we built a mask where the emission regions delimited in the $H\alpha$ frame have the constant value one and the rest are set to zero. Each broad-band image is then multiplied by this mask. Finally we perform aperture photometry on these images, to derive magnitudes and colors of each knot.

Table 5 shows the broad-band photometry of the sixteen knots detected in Mrk 370; the measurements have been corrected from Galactic extinction using the data published by Burstein & Heiles (1984). The extinction coefficient in the other bands were related to the B value following Rieke & Lebofsky (1985).

In order to characterize the stellar population of the individual regions, we compare their integrated properties with the predictions of evolutionary synthesis models. This task is especially difficult in this case, because at least three different contributors are producing the observed light: the young stars, the gaseous nebula surrounding them, and the older stars underlying the ongoing

burst. Broad-band colors must be corrected from the contribution of these different factors before they can be compared with the model predictions. In order to derive the "true" colors of the starburst, we proceeded in the following way.

First, colors were corrected for interstellar reddening, using the value of $C(H\beta)$ derived from our long slit spectra. For those knots lacking spectroscopic data, we used the $C(H\beta)$ averaged over the whole long-slit spectrum (which is probably our best possible guess).

Second, we have corrected for the contribution of emission lines. In gas rich objects, like BCDs, the presence of strong emission lines in the spectra can severely affect broad-band colors; the exact amount of the contribution of the lines to the flux observed in a given filter depends on the equivalent width of the line and on its precise location under the filter transmission profile. We used our spectroscopic information to compute the fraction of flux in the observed broad-band filters accounted for by each emission line, by using the task *calphot* in the *synphot* package of STSDAS.

Last, we subtracted the emission of the underlying population of stars. We assumed that the galaxy is composed of the starburst regions delimited by the FOCAS task, and of an underlying low surface brightness component, which is described by an exponential function (see next section).

The integrated magnitude of a knot, in a given band, λ , is given by:

$$m_\lambda = -2.5 \times \log (C_\lambda^{SB} + C_\lambda^D) + K_\lambda \quad (4)$$

where C_λ^{SB} is the number of counts in the knot coming from the starburst; C_λ^D is the contribution of the underlying disk within the knot region, and K_λ is the corresponding calibration constant (which incorporates exposure time, airmass, etc.).

C_λ^D is easily computed from the central surface brightness and scale length of the best-fit exponential model, and subtracted out in the previous formula, yielding the corrected magnitude of each knot:

$$m_\lambda(SB) = -2.5 \times \log (C_\lambda^{SB}) + K_\lambda \quad (5)$$

This process has been applied to the B , V , R and I bands. The images in U were not deep

enough to allow a reliable fit to the light profiles; however, by using typical values of $U-B$ for an evolved stellar population (Bruzual 1993; Vazdekis et al. 1996), we have estimated the contribution of the host galaxy in the U band. We found that, in this pass-band, the older component accounts for only $\sim 1\%$ of the knot flux, so we can neglect this correction. The resulting corrected colors are listed in Table 5.

We would like to stress that uncorrected and corrected knot colors differ significantly. In the case of the Mrk 370, while emission lines do not change much the broad band colors (shifts in $B-V$ are ≈ 0.05 or less), the internal extinction may change $B-V$ by up to 0.25 mag, and the effect of the contribution of the LSB stellar component is equally important. The final color shift is clearly function of the position in the galaxy; this means that it is dangerous to interpret color gradients as genuine variations of the knot properties (for instance their age) if the above corrections have not been applied.

4.2.2. The Underlying Stellar Population

Surface brightness profiles (SBP) in $BVRI$, as well as color profiles of Mrk 370, have been presented in Paper I. The SBP of the galaxy was used to decompose the galaxy in two components: the starburst, $H\alpha$ emitting regions, plus an older LSB stellar host. By fitting an exponential function to the faint, outer parts of the galaxy light profile (where we expect no or only negligible contribution from the starburst), we determined the structural parameters (scale length α and central surface brightness μ_0) of the LSB host. These parameters were used to calculate its total magnitudes in the different bands.

The structural parameters in the different bands, together with the total luminosities of the starburst and of the old stellar component, are given in Table 6.

Colors of the underlying component were derived from the best-fit exponential model; we found $(B-V)_{\text{host}} = 0.80$, $(V-R)_{\text{host}} = 0.50$ and $(V-I)_{\text{host}} = 1.46$.

5. Evolutionary properties of Mrk 370

5.1. The Starburst

In order to constrain the properties of the individual H II regions, we compare their observed properties with the predictions of *evolutionary population synthesis models*. These models assume that stars are born with masses distributed according to the initial mass function (IMF), with a star formation rate (SFR). The stars are evolved according to theoretical evolutionary tracks and finally, using empirical or theoretical calibrations, the predicted colors or spectra of the composite population are obtained. In the last years, people have been doing a lot of work in evolutionary synthesis models, see for instance Leitherer et al. (1996). Depending on the hypothesis on which the different models are based, the predicted values for the observables can be slightly different (for example, theoretical modeling of the evolution of massive star is still undergoing significant changes, Maeder & Conti 1994; and revision of these models often leads to new generations of synthesis calculations). This means that it is important to examine the characteristics of the available models and select the one most suitable to each specific case.

We have compared the derived observables of the starburst with the predictions of Leitherer et al. (1999, hereafter SB99) evolutionary synthesis models, known as *Starburst99*. These models provide a wide set of predictions for the spectrophotometric properties of star-forming galaxies. They are an improved version of the ones previously published by Leitherer & Heckman (1995): the latest set implements the stellar evolution models of the Geneva group, as well as the model atmosphere grid compiled by Lejeune, Cuisinier, & Buser (1997).

For each of the sixteen delimited knots, we searched for the model which best matches the observed parameters: $W(H\alpha)$, $U-B$, $B-V$, $V-R$ and $V-I$. In order to break the age and metallicity degeneration, we set the metallicity equal to that derived from the emission line fluxes (which is a reasonable approximation to the metallicity of a young population).

We found that, for all the knots, we can reproduce the observed quantities with an instantaneous burst (IB) of star formation and the Salpeter

IMF with an upper mass limit of $100 M_{\odot}$. No restriction can be put on the lower mass, given its poor sensitivity to the young burst evolution, which is dominated by the contribution of massive stars ($M > 8M_{\odot}$). The derived ages from $U-B$ and $H\alpha$ are quoted in Table 7; both observables give usually ages consistent with each other.

The ages derived using $B-V$, $V-R$ and $V-I$ are slightly larger, but in general compatible with the former. We notice that these colors are not very sensitive to the evolution of the young stars, as they vary by about 0.3 to 0.4 mag when the age increases from 0 to 100 Myr (SB99). Also, these colors are strongly contaminated by the different factors described in Section 4.2.1 (reddening, contribution of emission lines and emission of the older stars).

Although we have attempted to correct for such factors, the results might be imprecise due to the various hypotheses we made to work them out. First, we adopted a constant $C(H\beta)$ in those zone having no spectral information, while there may be spatial variations in the dust distribution, and $C(H\beta)$ can vary from knot to knot. That this is likely the case is shown by the results we obtained for the two central knots: $C(H\beta)_A = 0.31$ and $C(H\beta)_B = 0.39$, which translates into $E(B-V)_A = 0.22$, and $E(B-V)_B = 0.27$, and $E(V-I)_A = 0.34$ and $E(V-I)_B = 0.43$. If such variations are detected in two knots so close to each other, we can expect larger differences for the more peripheral knots. The same result is obtained from 2D spectroscopy: the 2D distribution of $C(H\beta)$ do not present an homogeneous morphology (see Figure 4), but larger $C(H\beta)$ close to the center of the star-forming knots.

The same applies to the contribution of emission lines, though, as mentioned earlier, they play a secondary role.

Furthermore, the uncertainties in the structural parameters obtained by the exponential fit of the LSB component also translate into uncertainties in the resultant colors.

All in all, the combined errors on the knot colors due to the various factors here discussed can be easily as large as 0.2 – 0.3 mag; this fact, together with their low sensitivity to the starburst properties, imply that $B-V$, $V-R$ and $V-I$ alone can not constrain the properties of the young stellar

population.

On the other hand, $U-B$ and $H\alpha$ are much more sensitive to the evolution of the young stars. They drastically change during the first million years of the stars life (see Figures 55, 56, 83 and 84 in SB99), which converts them in reliable indicators of the properties of star-forming regions.

We remark that none of the observable parameters will constrain accurately the properties of a star-forming region, unless we correct properly for the factors described above. The parameters measured directly (i.e. without correction) usually do not fit the models, and, if they do, they tend to give much older ages. This point is illustrated in Figures 8 and 9.

5.2. Age of the older stars

The $V-I$ color appears to be much too red to be compatible with a normal older stellar population. The data in the I band are not as good and deep as in the other bands, and the large uncertainties on the I -band structural parameters may be responsible for this discrepancy. Thus, the final ages have been derived by using the $B-V$ and $V-R$ colors. These colors have not been corrected from interstellar extinction, because the extinction coefficients we derived were based on the gas emission lines, and they may not apply to the regions outside the area occupied by the starburst. We have assumed that the metallicity of the stellar population is lower than the metallicity derived for the gas.

We have compared the $B-V$ and $V-R$ colors derived for the LSB component with the predictions of two different groups of evolutionary synthesis models:

The Galaxy Isochrone Synthesis Spectral Evolutionary Library, GISSEL 96 (Leitherer et al. 1996; Bruzual & Charlot 1993), which include simple stellar populations (SSP) or IB with different metallicities from $Z = 0.0004$ to $Z = 0.10$. The age varies from 0 to 20 Gyr, and Salpeter and Scalo IMFs are considered. We have also used the previous version of the models (GISSEL 95) in order to include a constant star forming rate (CSFR) — only available for solar metallicity.

The Spectrophotometric Population Synthesis Library for Old Stellar Systems (Vazdekis et al. 1996), a set of stellar population synthesis mod-

els designed to study old stellar systems. They synthesize SSP or follow the galaxy through its evolution from an initial gas cloud to the present time, assuming an analytical functional form for the SFR (see Section 3.1 in Vazdekis et al. 1996), and including the chemical evolution. Two different IMFs are considered: a unimodal IMF, with a power law form whose slope is a free parameter, and a bimodal IMF, equal to the unimodal IMF for stars with masses above $0.6 M_{\odot}$, but with a reduced influence of the stars with lower masses.

When comparing with the predictions of the IB approximation, both models give ages of ~ 5 Gyr for the older stellar component of Mrk 370.

However, when changing the star forming history, we obtained different results. the $B-V$ and $V-R$ colors could not be reproduced by GIS-SEL95 with a CSFR. Next, we applied Vazdekis et al. (1996) models, which include chemical evolution. We considered Salpeter IMF, and the different ν (ν is a constant fixing the timescale of star formation, see Sect 3.1 in Vazdekis et al. 1996), provided by the models. We found the following results: when $\nu = 1$ the observed colors are inconsistent with the predictions of the models; with $\nu = 5$ colors agree with ages between 9 and 11 Gyr; and in the rest of the cases ($\nu = 10, 20$ and 50) colors are consistent with ages between 4 and 7 Gyrs.

Optical colors are not very sensitive to the evolution of the older stars; for instance, $B-V$ increase by ≈ 0.1 mag when ages varies from 5 to 17 Gyr and the same applies to $V-R$. Such variations are of the order of the uncertainties in our measured colors. Although no firm constraints could be put on the age of the underlying stellar population, the above comparison with models point to a minimum age of 5 Gyrs; but it is clear that in order to better constrain the age of the LSB host, it is indispensable to include near-infrared colors in the analysis.

6. Discussion

It turns out from the above results that the kind of spectrophotometric study we have carried out is fundamental in order to disentangle the stellar populations in BCDs and derive their star forming histories. However, as we have already pointed out in the introduction, most of the work carried

out so far has focused on statistical analysis of BCDs samples, while only a few papers have been devoted to examining in detail the characteristic of individual objects:

The two extremely compact and low-metallicity BCDs, SBS 0335-052 and Tololo 65, both classified as i0 (LT86), have been the subject of recent spectrophotometric studies by Papaderos et al. (1998, 1999). They found in both cases that the properties of the underlying component are consistent with those of a stellar population not older than one Gyr.

Noeske et al. (2000) report on results from a spectrophotometric analysis of two iI,C ("Cometary BCDs", LT86) Mrk 59 and Mrk 71. Spectral population synthesis models, in combination with color magnitudes diagrams and color profiles, yield a most probable formation age of ≈ 2 Gyr for the old stars in both galaxies. Two other cometary BCDs have been studied by Fricke et al. (2001) — Tololo 1214-277 — and Guseva et al. (2001) — SBS0940+544. In the latter case, no compelling evidences favor either a young or an old age.

Despite the fact that nE/iEs are the most common type of BCD, there are very few studies, with the same quality, of objects belonging to this class. Steel et al. (1996) and Méndez et al. (1999) have performed spectrophotometric observations of the iE BCDs Haro 3 and II Zw 33 respectively. Although in both cases an underlying component of older stars was detected, their data did not permit to determine its properties, and both studies limited the analysis to the young starburst. The ages and star-forming scenarios they found for these two objects are consistent with our findings. They also found metallicities comparable to the metallicity we have derived for Mrk 370. More recently, a comprehensive analysis of the iE BCD galaxy Mrk 86 has been published by Gil de Paz et al. (2000) and Gil de Paz, Zamorano, & Gallego (2000). They studied the properties of 46 individual star-forming knots as well as the underlying population of older stars. By applying evolutionary synthesis models, they found that three well defined stellar populations are present in Mrk 86: the star-forming regions, with ages between 5 and 13 Myr, and no significant age or metallicity gradient, a central starburst with an intermediate age of 30 Myr, and an underlying population of stars, with a surface brightness profile that can be de-

scribed by an exponential, with no color gradients and an age between 5 and 13 Gyrs.

In all the above studies the star-forming knots present a similar range of ages, consistent with our findings for Mrk 370. However, the galaxies appear to be different with respect to the properties of their underlying population of stars: while i0 and cometary BCDs seem to be less evolved systems, the structural properties and ages derived for the LSB of Mrk 370 are quite similar to those presented by the iE BCD Mrk 86. This fact may imply that BCDs are objects which have in common the presence of an active starburst, which dominates their optical properties but, when the characteristics of the underlying stellar component are taken into account, they form a more heterogeneous class. This picture could naturally explain the different evolutionary stages derived for the galaxies.

We argue that considering BCD as a class might be then inappropriate. Therefore, looking for absolute unifying scenarios — for instance, trying to link the whole BCD class with the different types of dwarf galaxies (when only a fraction of them could be actually connected) — may be speculative at this time.

On the other hand, Noeske et al. (2000) suggested that an evolutionary sequence might exist connecting the different BCD subtypes, the iI,C galaxies being a possible link between the extremely young galaxy candidates (iO class) and the more evolved iE/nE BCDs.

The information available at the present time does not permit to discard any of these hypothesis. Comprehensive studies of larger samples of BCDs are required in order to find out which scenario is the correct one.

Our kinematic results suggest ordered motion around the north-south axis of Mrk 370, the kinematic center being located close to the center of the external isophotes; this could imply that the gas is rotating coupled with the main body of the galaxy (the underlying population hosting the starburst). However, we should take into account that, because of our limited spectral resolution, more complex gas motions could escape detection. In fact, Östlin et al. (1999, 2001), analyzing high-resolution (velocity sampling $\simeq 5 \text{ km sec}^{-1}$) Fabry-Perot observations of BCD galaxies, found

that, in general, the velocity fields of the studied galaxies are irregular and distorted. Spectroscopic observations of Mrk 370 with high velocity resolution are needed to better trace its gas kinematics.

Besides, Mrk 370 present some other puzzling peculiarities: the peak in the continuum map does not coincide with the kinematic center, nor with the center of the outer isophotes, nor with one of the knots; and the position angle of the outer regions, seen in the *R*-band grey-scale map, differs by about 30 degrees from the position angle displayed by the $\text{H}\alpha$ map.

7. Summary and Conclusions

Broad- and narrow- band images of the BCD Mrk 370, together with long-slit and two-dimensional spectra, have been analyzed in order to derive the properties of the different components of the galaxy and to constrain its evolutionary status. Our results can be summarized as follow:

- Two different stellar components are clearly distinguished in the galaxy: the present starburst and an underlying older population. The current star formation activity takes place in numerous knots, aligned in a north-east south-west direction. An extended LSB component, with regular appearance, hosts this star-forming area.
- The oxygen abundance derived from the spectra is $Z \simeq Z_\odot/2$, a value relatively high for the BCD class; the high blue continuum, the absorption wings in the Balmer lines and the pronounced Balmer discontinuity in its spectrum are clear indicators of the presence of an evolved stellar population.
- The starburst region is resolved into small and compact star-forming regions. We identified a total of sixteen knots, and derived their individual properties. The brightest knots have luminosities similar to those of giant H II regions in M33 and in the LMC. The photometric parameters of the individual star-forming knots were corrected from the contribution of emission lines, internal extinction and emission from the underlying LSB component. The colors before and after the corrections are significantly different.

In Mrk 370 the internal extinction and the contribution of older stars are more important than emission lines in shifting the observed broad-band colors of the knots. The color shifts are function of the position of the knot in the galaxy, and we strongly caution against interpreting observed color gradients as age gradients *before* applying such corrections.

We found that we can reproduce the colors of all the knots with an IB of star formation and the Salpeter initial mass function (IMF) with an upper mass limit of $100 M_{\odot}$. The ages of the knots range between 3 and 6 Myrs.

- The age of the underlying stellar population has been estimated by comparing its optical colors with two different groups of evolutionary synthesis models. Colors are consistent with ages larger than 5 Gyr.
- The inner, brightest star forming-regions, previously cataloged as double nucleus, are normal H II regions. We would like to stress that the "multiple nuclei" often seen in broad-band images of BCD galaxies may be just the superposition of off-center luminous H II regions. If Mrk 370 is not a double-nucleus galaxy, then there may be no compelling evidence that it has experienced recent interactions. Indeed, there are no other signs of interactions; the regularity of the velocity field, and the fact that the central knots share the same kinematics of the main body point against a recent merger or interaction event. Also, Noeske et al. (2001) report that Mrk 370 is an isolated galaxy.
- We obtained the mean ionized gas velocity field in the central part of the galaxy. The velocity field seems to be regular and similar to that of a rotating disk (west region approaching, east region receding).

All in all, spectrophotometric studies of BCDs are of paramount importance in order to derive their evolutionary status. These analyses must include, in addition to the whole optical dataset, near-infrared photometry (NIR) — colors in the NIR better trace the properties of the older stellar

component — as well as deep optical spectrophotometry of the host galaxy. Besides, high resolution spectroscopy of BCDs will help trace the kinematics of the galaxy and provide valuable information on the mechanisms triggering the star formation.

Based on observations with the JKT, INT and WHT, operated on the island of La Palma by the Royal Greenwich Observatory in the Spanish Observatorio del Roque de los Muchachos of the Instituto de Astrofísica de Canarias. Based also on observations taken at the German-Spanish Astronomical Center, Calar Alto, Spain, operated by the Max-Planck-Institut für Astronomie (MPIA), Heidelberg, jointly with the spanish "Comisión Nacional de Astronomía". We thank the staff of both observatories. This research has made use of the NASA/IPAC Extragalactic Database (NED), which is operated by the Jet Propulsion Laboratory, Caltech, under contract with the National Aeronautics and Space Administration.

We thank J. Iglesias-Páramo and J.N. González-Pérez for their help in the initial stages of this project. We thank A. Vazdekis, P. Papaderos and K. Noeske for valuable comments and discussions. We also acknowledge the anonymous referee for his/her helpful comments which helped us improve this paper.

This work has been partially funded by the spanish "Ministerio de Ciencia y Tecnología" (grants AYA2001-3939 and PB97-0158). L.M. Cairós acknowledges support by the EC grant HPMF-CT-2000-00774.

REFERENCES

Arribas, S., Carter, D., Cavaller, L., del Burgo, C., Edwards, R., Fuentes, F. J., García, A. A., Herreros, J. M., Jones, L. R., Mediavilla, E., Pi, M., Pollacco, D., Rasilla, J. L., Rees, P. C., Sosa, N. A., et al. 1998, Proc. SPIE, 3355, 821

Bingham, R. G., Gellatly, D. W., Jenkins, C. R., & Worswick, S. P. 1994, Proc. SPIE, 2198, 56

Brocklehurst, M. 1971, MNRAS, 153, 471

Bruzual, A. G. 1993, Revista Mexicana de Astronomía y Astrofísica, vol. 26, 26, 126

Bruzual, A. G. & Charlot, S. 1993, ApJ, 405, 538

Burstein, D. & Heiles, C. 1984, *ApJS*, 54, 33

Cairós, L. M. 2000, PhD Thesis

Cairós, L. M., Vílchez, J. M., Gómez-Pérez, J. N., Iglesias-Páramo, J., & Caon, N. 2001a, *ApJS*, 133, 321 (= Paper I)

Cairós, L. M., Caon, N., Vílchez, J. M., Gómez-Pérez, J. N., & Muñoz-Tuñón, C. 2001b, *ApJS*, 136, 2 (= Paper II)

Cananzi, K., Augarde, R., & Lequeux, J. 1993, *A&A*, 101, 599

Coziol, R. 1996, *A&A*, 309, 345

Davies, J. I. & Phillipps, S. 1988, *MNRAS*, 233, 553

Díaz, A. I. 1988, *MNRAS*, 231, 57

Doublier, V., Comte, G., Petrosian, A., Surace, C., & Turatto, M. 1997, *A&AS*, 124, 405

Doublier, V., Caulet, A., & Comte, G. 1999, *A&AS*, 138, 213

Falco, E., Kurtz, M., Gellar, M., Huchra, J., Peters, J., Berlind, P., Mink, D., Tokarz, S., & Elwell, B. 2000, The Updated Zwicky Catalog (UZC)

Fricke, K. J., Izotov, Y. I., Papaderos, P., Guseva, N. G., & Thuan, T. X. 2001, *AJ*, 121, 169

Fuentes-Masip, O., Muñoz-Tuñón, C., Castañeda, H. O., & Tenorio-Tagle, G. 2000, *AJ*, 120, 752

García-Lorenzo, B., Mediavilla, E., & Arribas, S. 1999, *ApJ*, 518, 190

Gil de Paz, A., Zamorano, J., & Gallego, J. 2000, *A&A*, 361, 465

Gil de Paz, A., Zamorano, J., Gallego, J., & Domínguez, F. 2000, *A&AS*, 145, 377

Gerola, H., Seiden, P. E., & Schulman, L. S. 1980, *BAAS*, 12, 528

Guseva, N. G. et al. 2001, *A&A*, 378, 756

Kennicutt, R. C., Jr. 1988, *ApJ*, 334, 144

Kennicutt, R. C., Jr. 1991, in IAU Symp. 148, The Magellanic Clouds, ed. R. Haynes, D. Milne (Dordrecht: Kluwer), 139

Kunth, D. & Östlin, G. 2000, *A&A Rev.*, 10, 1

Landolt, A. U. 1992, *AJ*, 104, 340

Leitherer, C. & Heckman, T. M. 1995, *ApJS*, 96, 9

Leitherer, C. et al. 1996, *PASP*, 108, 996

Leitherer, C. et al. 1999, *ApJS*, 123, 3

Lejeune, T., Cuisinier, F., & Buser, R. 1997, *A&AS*, 125, 229

Loose, H. H. & Thuan, T. X. 1986, in Star Forming Dwarf Galaxies and Related Objects, eds. D. Kunth, T. X. Thuan, J. T. T. Van (Gif-sur-Yvette: Editions Frontières), 73 (= LT86)

Maeder, A. & Conti, P. S. 1994, *ARA&A*, 32, 227

Maíz-Apellaniz, J., Mas-Hesse, J. M., Muñoz-Tuñón, C., Vílchez, J. M., & Castañeda, H. O. 1998, *A&A*, 329, 409

Marlowe, A. T., Meurer, G. R., Heckman, T. M., & Schommer, R. 1997, *ApJS*, 112, 285

Marlowe, A. T., Meurer, G. R., & Heckman, T. M. 1999, *ApJ*, 522, 183

Mazzarella, J. M. & Boroson, T. A. 1993, *ApJS*, 85, 27

McCall, M. L., Rybski, P. M., & Shields, G. A. 1985, *ApJS*, 57, 1

McGaugh, S. S. 1991, *ApJ*, 380, 140

Mediavilla, E., Arribas, S., del Burgo, C., Osocoz, A., Serra-Ricart, M., Alcalde, D., Falco, E. E., Goicoechea, L. J., García-Lorenzo, B., & Buitrago, J. 1998, *ApJ*, 503, L27.

Méndez, D. I., Cairós, L. M., Esteban, C., & Vilchez, J. 1999, *AJ*, 117, 1688

Mihalas, D. & Binney, J. 1981, *Science*, 214, 829

Noeske, K. G., Guseva, N. G., Fricke, K. J., Izotov, Y. I., Papaderos, P., & Thuan, T. X. 2000, *A&A*, 361, 33

Noeske, K. G., Iglesias-Páramo, J., Vilchez, J. M., Papaderos, P., & Fricke, K. J. 2001, *A&A*, 371, 806

Nordgren, T. E., Helou, G., Chengalur, J. N., Terzian, Y., & Khachikian, E. 1995, ApJS, 99, 461

Oke, J. B. 1990, AJ, 99, 1621

Olofsson, K. 1995, A&A, 111, 57

Östlin, G. 1998, Ph.D. Thesis

Östlin, G., Amram, P., Masegosa, J., Bergvall, N., & Boulesteix, J. 1999, A&AS, 137, 419

Östlin, G., Amram, P., Bergvall, N., Masegosa, J., Boulesteix, J., & Márquez, I. 2001, A&A, 374, 800

Pagel, B. E. J., Edmunds, M. G., Blackwell, D. E., Chun, M. S., & Smith, G. 1979, MNRAS, 189, 95

Papaderos, P., Loose, H.-H., Thuan, T. X., & Fricke, K. J. 1996a, A&AS, 120, 207

Papaderos, P., Loose, H.-H., Fricke, K. J., & Thuan, T. X. 1996b, A&A, 314, 59

Papaderos, P., Izotov, Y. I., Fricke, K. J., Thuan, T. X., & Guseva, N. G. 1998, A&A, 338, 43

Papaderos, P., Fricke, K. J., Thuan, T. X., Izotov, Y. I., & Nicklas, H. 1999, A&A, 352, L57

Rieke, G. H. & Lebofsky, M. J. 1985, ApJ, 288, 618

Sargent, W. L. W. & Searle, L. 1970, ApJ, 162, L155

Skillman, E.D. & Kennicutt, R. C., Jr. 1993, ApJ, 411, 655

Steel, S. J., Smith, N., Metcalfe, L., Rabbette, M., & McBreen, B. 1996, A&A, 311, 721

Telles, J. E. 1995, Ph.D. Thesis

Thuan, T. X. & Martin, G. E. 1981, ApJ, 247, 823

Thuan, T. X. 1985, ApJ, 299, 881

Thuan, T. X. 1991, in *Massive Stars in Starburst*. In: Leitherer C., Walborn N.R., Heckman T.M., Norman C.A. (eds). Cambridge: Cambridge University Press, p. 183

Vazdekis, A., Casuso, E., Peletier, R. F., & Beckman, J. E. 1996, ApJS, 106, 307

Whitford, A.E. 1958, AJ, 63, 201

TABLE 1
BASIC DATA OF MRK 370

Galaxy	Other designations	R.A. (1950)	Dec.	M_B	D (Mpc)	M_{HI}^1	M_T^1
Mrk 370	NGC 1036, UGC 02160	02 ^h 37 ^m 40 ^s	19° 05' 01"	-17.20	12.9	0.36×10 ⁹	4.2 × 10 ⁹

NOTE.—(1) Neutral hydrogen mass M_{HI} and total mass M_T in units of M_\odot ; both from Thuan and Martin (1981).

TABLE 2
LOG OF THE OBSERVATIONS

Date	Telescope	Instrument	Filter/grism	Exposure time (s)
Oct. 98	JKT 1.0m	Cass. focus	U	2400
Oct. 98	JKT 1.0m	Cass. focus	B	1500
Oct. 98	JKT 1.0m	Cass. focus	V	1000
Oct. 98	JKT 1.0m	Cass. focus	R	800
Oct. 98	JKT 1.0m	Cass. focus	I	1200
Dec. 97	CAHA 2.2m	CAFOS	6569 (113)	5400
Dec. 97	CAHA 2.2m	CAFOS	6462 (98)	5400
Sep. 98	INT 2.5m	IDS	R300V	1800
Aug. 99	WHT 4.2m	INTEGRAL	600g/mm	3600

NOTE.— JKT = Jacobous Kapteyn Telescope, ORM (La Palma), Spain (detector: Tek 1024×1024, 0''.33/pixel). CAHA = Centro Astronómico Hispano Alemán, Almería, Spain (Site-1D 2048×2048, 0''.53/pixel)/ INT = Isaac Newton Telescope, ORM (La Palma), Spain (EEV10 4100 × 2048 13.5 μ pixels). WHT = William Herschel Telescope, ORM (La Palma), Spain (Tex 1024 × 1024 24 μ pixels).

TABLE 3
REDDENING CORRECTED LINE INTENSITY RATIOS

Line (Å)	Ion	$f(\lambda)$	A		B		S	
			F_λ	$-W_\lambda$	F_λ	$-W_\lambda$	F_λ	$-W_\lambda$
3727	[O II]	0.26	2.74 ± 0.06	35.1 ± 0.9	3.22 ± 0.09	136 ± 10	2.68 ± 0.04	48 ± 1
3869	[Ne III]	0.23	0.50 ± 0.07	5.1 ± 0.8	1.1 ± 0.2	330 ± 166	0.49 ± 0.06	7 ± 1
4101	H δ	0.18	0.28 ± 0.03	2.1 ± 0.4	0.24 ± 0.04	7 ± 1	0.26 ± 0.02	2.5 ± 0.3
4340	H γ	0.14	0.45 ± 0.02	3.0 ± 0.2	0.50 ± 0.02	14.0 ± 0.8	0.49 ± 0.07	5 ± 1
4861	H β	0	1.00 ± 0.01	12.6 ± 0.1	1.00 ± 0.02	26.9 ± 0.8	1.00 ± 0.01	16.0 ± 0.3
4959	[O III]	-0.02	0.53 ± 0.01	6.1 ± 0.2	0.60 ± 0.02	15.5 ± 0.6	0.52 ± 0.01	7.6 ± 0.1
5007	[O III]	-0.03	1.60 ± 0.02	19.2 ± 0.2	1.93 ± 0.03	51.2 ± 0.6	1.63 ± 0.02	25.0 ± 0.2
5876	HeI	-0.23	0.06 ± 0.01	0.8 ± 0.1	0.10 ± 0.01	3.5 ± 0.3	0.069 ± 0.006	1.3 ± 0.1
6548	[N II]	-0.34	0.14 ± 0.01	2.5 ± 0.2	0.11 ± 0.01	4.2 ± 0.6	0.149 ± 0.008	3.4 ± 0.2
6563	H α	-0.34	2.85 ± 0.05	56.8 ± 0.6	2.93 ± 0.09	112 ± 2	2.86 ± 0.03	68.1 ± 0.7
6584	[N II]	-0.34	0.50 ± 0.02	10.1 ± 0.5	0.49 ± 0.02	24 ± 2	0.476 ± 0.009	11.6 ± 0.3
6678	He I	-0.35	0.04 ± 0.02	0.8 ± 0.4	0.06 ± 0.03	3 ± 1	0.030 ± 0.008	0.7 ± 0.2
6717	[S II]	-0.36	0.50 ± 0.01	10.0 ± 0.2	0.45 ± 0.02	21.3 ± 0.9	0.471 ± 0.008	11.5 ± 0.2
6731	[S II]	-0.36	0.38 ± 0.01	7.4 ± 0.3	0.34 ± 0.02	17 ± 2	0.365 ± 0.007	9.0 ± 0.2
7135	[Ar III]	-0.41	0.11 ± 0.01	2.4 ± 0.4	0.10 ± 0.01	4.9 ± 0.8	0.093 ± 0.006	2.5 ± 0.2
$C(H\beta)$		0.31 ± 0.02		0.39 ± 0.03		0.285 ± 0.004		
$W_{\text{abs}}(\text{\AA})$		1.3		0.0		1.4		
$F(H\beta)$		2.67 ± 0.0014		1.55 ± 0.12		3.87 ± 0.06		

NOTE.—Reddening-corrected line intensities (normalized to H β = 1) for the regions extracted from the long slit spectrum of Mrk 370. The integrated spectrum S is presented in the rightmost columns. Balmer lines are corrected from underlying stellar absorption. The reddening coefficient, $C(H\beta)$, the value of the absorption correction, W_{abs} , and the measured H β flux, $F(H\beta)$ ($\times 10^{-14}$ erg cm $^{-2}$ sec $^{-1}$) are also included.

TABLE 4
 $\text{H}\alpha$ PHOTOMETRY OF THE INDIVIDUAL KNOTS IN MRK 370

Knot	Flux($\text{H}\alpha$)	$\log L(\text{H}\alpha)$	$\log N_{Ly\alpha}$	$\log(M_{HII}/M_{\odot})$	$-W(\text{H}\alpha)$	$-W(\text{H}\alpha)_{\text{corr}}$
1	5.70	38.05	49.92	3.13	201	364
2	1.96	37.59	49.46	2.67	170	534
3	5.08	38.00	49.87	3.08	138	260
4	8.01	38.20	50.01	3.28	173	329
5	4.13	37.91	49.78	2.99	45	71
6	0.68	37.13	49.00	2.20	94	...
7	1.64	37.51	49.38	2.59	38	116
8	37.30	38.87	50.74	3.95	58	63
9	7.29	38.16	50.03	3.24	81	119
10	4.56	37.96	49.82	3.03	114	578
11	147.07	39.47	51.33	4.64	373	533
12	232.17	39.66	51.53	4.96	192	226
13	2.32	37.66	49.53	2.74	71	...
14	33.31	38.82	50.69	3.90	237	579
15	4.01	37.90	49.77	2.98	73	223
16	5.39	38.03	49.90	3.11	220	656

NOTE.—The data are corrected from interstellar extinction and from [N II] emission. The equivalent widths are shown before and after correction from the contribution of the underlying stellar emission to the underlying continuum (except knots 6 and 13). $\text{H}\alpha$ fluxes are in 10^{-15} erg cm^{-2} sec^{-1} units; $\text{H}\alpha$ luminosities in erg sec^{-1} units. $W(\text{H}\alpha)$ in Amstrongs

TABLE 5
BROAD-BAND PHOTOMETRY OF THE INDIVIDUAL KNOTS DETECTED IN MRK 370.

Knot	<i>B</i>	<i>U</i> − <i>B</i>	<i>B</i> − <i>V</i>	<i>V</i> − <i>R</i>	<i>V</i> − <i>I</i>	<i>B</i> _c	(<i>U</i> − <i>B</i>) _c	(<i>B</i> − <i>V</i>) _c	(<i>V</i> − <i>R</i>) _c	(<i>V</i> − <i>I</i>) _c
1	20.19	−0.57	0.39	0.25	0.88	19.67	−0.94	0.05	0.04	0.24
2	21.01	−0.56	0.33	0.38	1.01	20.70	−1.05	−0.14	0.23	0.26
3	20.15	−0.45	0.47	0.39	1.00	19.69	−0.88	0.12	0.21	0.47
4	19.88	−0.54	0.42	0.44	1.02	19.43	−0.97	0.05	0.30	0.47
5	19.28	−0.20	0.53	0.38	0.96	18.76	−0.57	0.24	0.17	0.45
6	21.82	−0.23	0.67	0.31	1.41	22.24	−1.54	0.14	−0.04	1.20
7	20.11	−0.09	0.60	0.41	1.07	19.88	−0.74	0.24	0.17	0.46
8	16.80	−0.42	0.28	0.29	0.66	16.04	−0.55	0.06	0.10	0.33
9	19.17	−0.20	0.50	0.40	0.94	18.56	−0.47	0.24	0.18	0.55
10	20.00	−0.24	0.57	0.47	1.13	19.73	−0.85	0.21	0.24	0.66
11	17.46	−0.65	0.33	0.39	0.69	17.37	−0.79	0.19	0.28	0.46
12	15.77	−0.45	0.31	0.33	0.66	14.80	−0.60	0.02	0.05	0.21
13	20.13	−0.11	0.56	0.48	1.06	19.97	−0.84	0.12	0.10	0.43
14	18.43	−0.56	0.35	0.41	0.82	17.90	−0.92	−0.01	0.14	0.17
15	19.81	−0.45	0.42	0.41	1.25	19.61	−1.14	−0.15	0.26	0.76
16	20.50	−0.48	0.32	0.47	0.84	20.21	−1.08	−0.28	0.45	−1.68

NOTE.—Columns 2 to 6: only the Galactic extinction correction has been applied; columns 7 to 11: values corrected from interstellar extinction, contribution of emission line and emission from the underlying host galaxy.

TABLE 6
STRUCTURAL PARAMETERS CHARACTERIZING THE LSB HOST.

Band	μ_0	α	M_{SB}	M_{host}	$R_{\text{SB}/\text{host}}$
B	22.56	1.06	-16.69	-16.13	1.68
V	21.74	1.05	-16.91	-16.93	0.98
R	21.04	0.96	-17.32	-17.44	0.89
I	20.57	1.14	-17.23	-18.28	0.38

NOTE.—Columns 2, 3: centrals surface brightness (mag arcsec $^{-2}$) and scale-length (kpc); column 3, 4: absolute magnitude of the starburst and of the host LSB in each band; column 5: the ratio of the luminosity of the starburst over the luminosity of the underlying component. As mentioned in the text, the U -band image was too shallow to reach out the outer, starburst-free regions.

TABLE 7
DERIVED AGES (IN MYR) FOR THE INDIVIDUAL STAR-FORMING KNOTS IN MRK 370

Knot	Age $_{U-B}$	Age $_{EW(\text{H}\alpha)}$	Knot	Age $_{U-B}$	Age $_{EW(\text{H}\alpha)}$
1	3.2–4.8	4.8–5.1	9	5.6–6.4	5.9–6.3
2	3.1–3.8	4.6–4.8	10	4.5–5.0	4.6–4.8
3	3.5–5.0	5.0–5.5	11	4.6–5.1	4.6–4.8
4	3.2–4.7	4.8–5.2	12	5.1–5.9	5.1–5.7
5	5.1–6.0	6.4–7.0	13	4.5–5.1	—
6	—	6.1–6.6	14	3.2–4.8	4.6–4.8
7	4.8–5.3	5.9–6.3	15	2.2–3.3	5.1–5.7
8	5.3–6.2	6.4–7.0	16	2.9–3.5	4.3–4.7

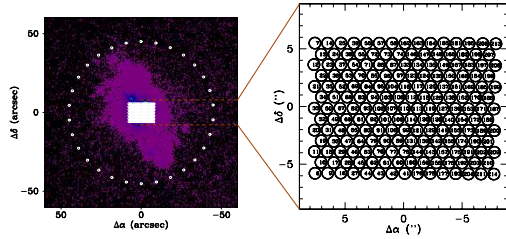


Fig. 1.— (left) Image of Mrk 370 through the H α filter, taken with the 2.2m telescope at CAHA. The spatial distribution of the fibers (SB2) on the focal plane has been overlaid. (right) Fibers in the central array. Numbers indicate the actual position of the fibers at the slit.

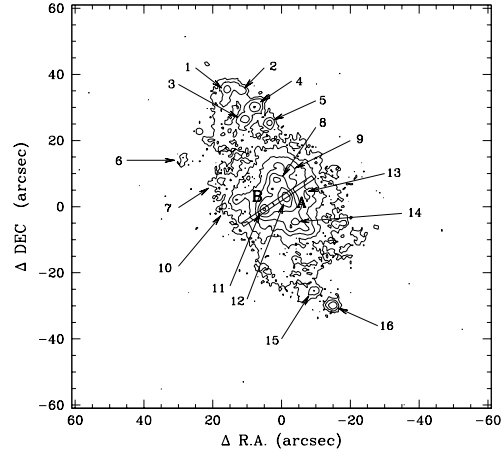


Fig. 2.— Contour plot of the continuum-subtracted H α image of Mrk 370. The slit position is indicated, and the two subregions selected in the long-slit spectrum are marked A and B. The individual star-forming regions are labeled. North is at the top and East is on the left.

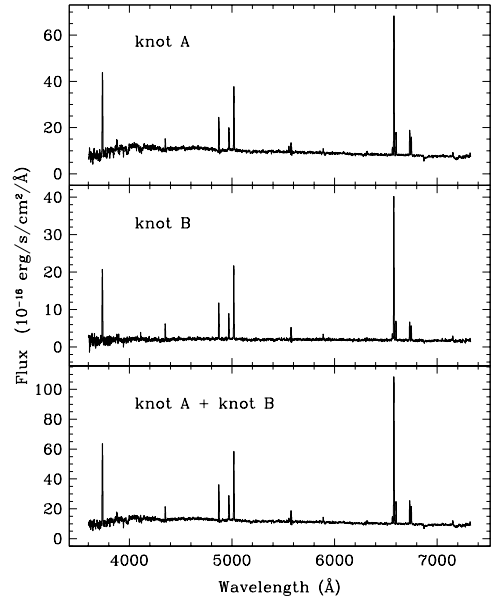


Fig. 3.— Spectra of regions A and B, and the total integrated spectrum (region S).

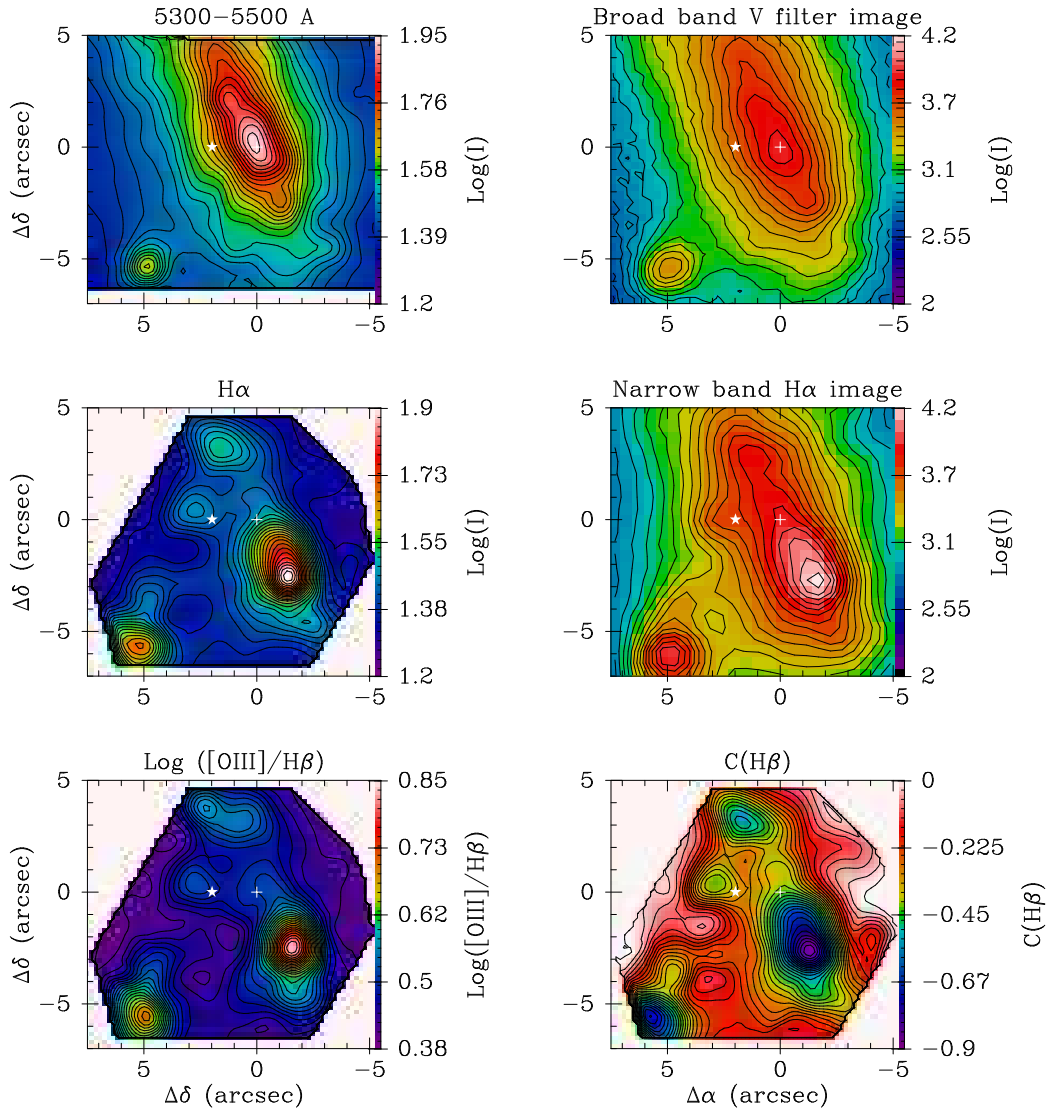


Fig. 4.— [from left to right, top to bottom] (a) Mrk 370 continuum map obtained from the 2D spectroscopic data by integrating the signal in the indicated spectral interval; (b) V filter image; (c) Intensity map of the H α emission line obtained by fitting a single gaussian to 2D spectroscopy data; (d) H α filter image from the 2.2m CAHA; (e) Two-dimensional distribution of [O III]/H β ratio; (f) Two-dimensional distribution of the extinction coefficient C(H β). A cross marks the optical nucleus in each map. The geometrical center of the outer isophotes is indicated by a star.

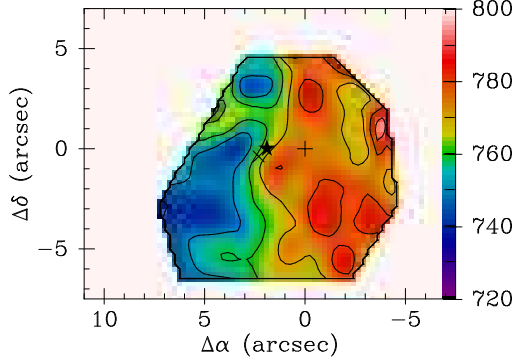


Fig. 5.— Velocity field of the ionized gas in the central region of Mrk 370, determined by averaging measurements from different emission lines. A black cross marks the optical nucleus. The kinematic center is indicated by an X. The center of the outer isophotes is indicated by a black star.

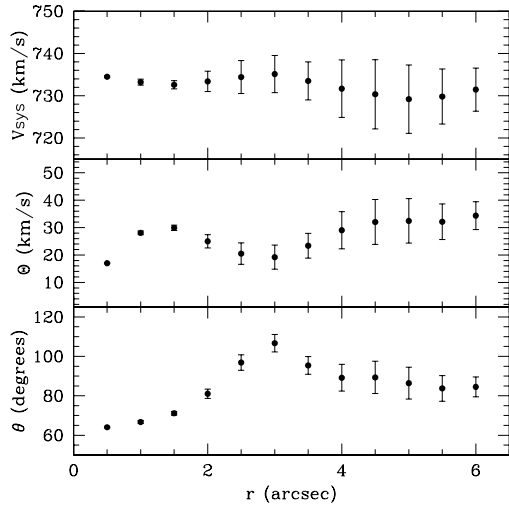


Fig. 6.— Radial dependence of the systemic velocity V_{sys} , amplitude of the velocity field projection on the galactic plane Ω , and position angle of the major kinematical axis δ . Error bars only reflect the local rms in the measurements, and do not reflect the actual uncertainties, which are likely affected by systematic errors.

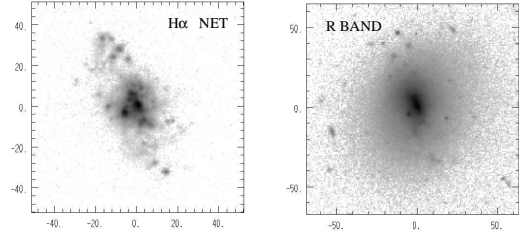


Fig. 7.— left panel: Continuum-subtracted $H\alpha$ grey-scale map of Mrk 370; right panel: R-band image. North is at the top and East is on the left; axis units are arcsec.

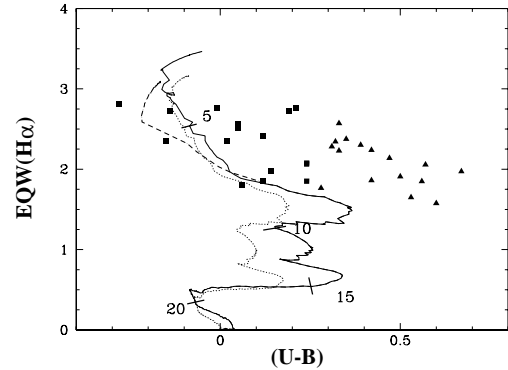


Fig. 8.— Equivalent width of the $H\alpha$ line *versus* $(U - B)$. We also plot the tracks of an instantaneous burst of $z = 0.008$, aged from 1 to 30 Myr (Leitherer et al. 1999), for three IMFs: solid line, $\alpha=2.35$, $M_{\text{up}}=100M_{\odot}$; dotted line: $\alpha=3.30$, $M_{\text{up}}=100M_{\odot}$; short-dash line, $\alpha=2.35$, $M_{\text{up}}=30M_{\odot}$. Triangles represent the observed (uncorrected) parameters of the individual knots; squares represent the knots parameters after applying the corrections from reddening and from the contribution of emission lines and older stars.

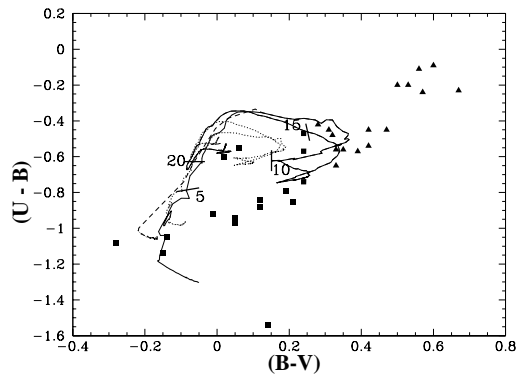


Fig. 9.— $(U - B)$ versus $(B - V)$. The track of an instantaneous burst of $z = 0.008$, aged from 1 to 30 Myr (Leitherer et al. 1999), are also plotted, for three different IMFs: solid line, $\alpha=2.35$, $M_{up}=100M_{\odot}$; dotted line: $\alpha=3.30$, $M_{up}=100M_{\odot}$; short-dash line, $\alpha=2.35$, $M_{up}=30M_{\odot}$. Symbols are the same as in the previous figure

8. APPENDIX A

8.1. Atlas of Spectra

The nuclear spectrum of Mrk 370 derived from the INTEGRAL data is shown in figure 10, in the whole wavelength range observed. We can easily recognize several emission lines. Here we only plot some of selected emission as spectrum diagrams (figures 11 through 14). Spectrum diagrams represent line profiles from individual spectra at each point in the observed region and in a small spectral range. The spectra at each location are normalized by the local peak so as to better display the profile shape (lines nearer to the bright knots are brighter than those farther out).

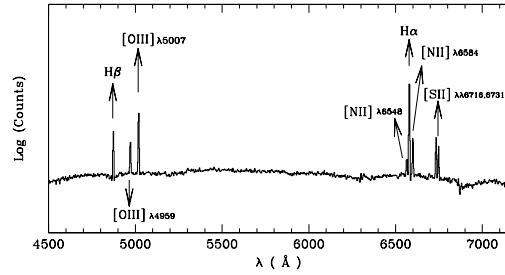


Fig. 10.— Nuclear spectrum of Mrk 370, obtained by averaging the 7 fibers closest to the continuum maximum ($r < 1''.2$).

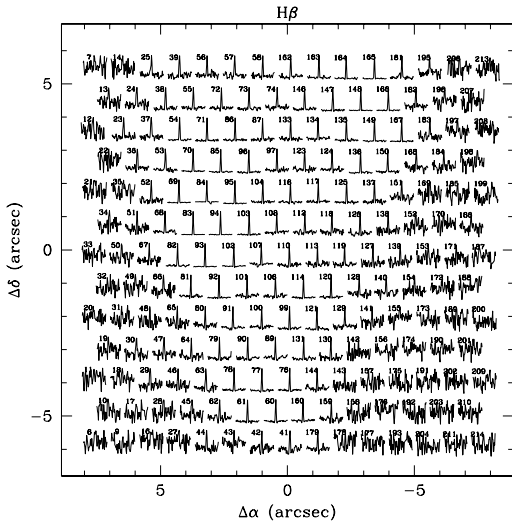


Fig. 11.— Spectra distribution diagrams of the central $16'' \times 12''$ of Mrk 370. Two-dimensional distribution of the $H\beta$ lines (the absorption wings are visible). The spectral range plotted is $4795-4950 \text{ \AA}$.

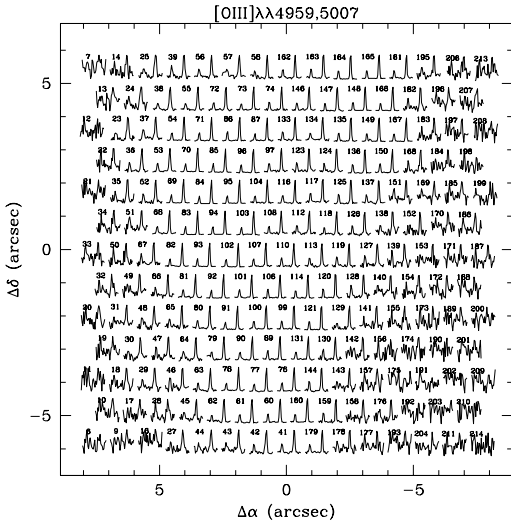


Fig. 12.— Two-dimensional distribution of $[\text{O III}]\lambda\lambda 4959+[\text{O III}]\lambda 5007$ (4950–5045 Å).

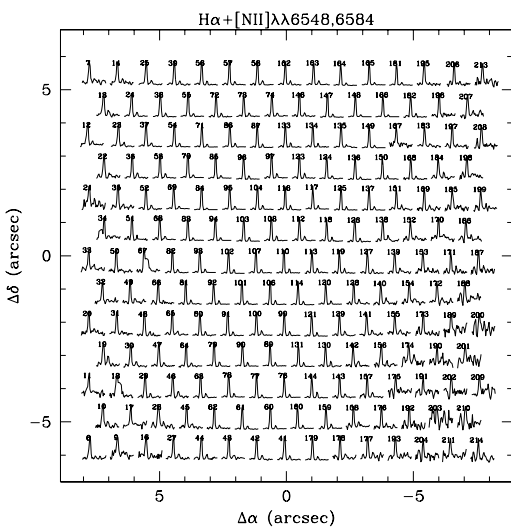


Fig. 13.— Two-dimensional distribution of $\text{H}\alpha+[\text{N II}]\lambda\lambda 6548, 6584$ (6550–6640 Å).

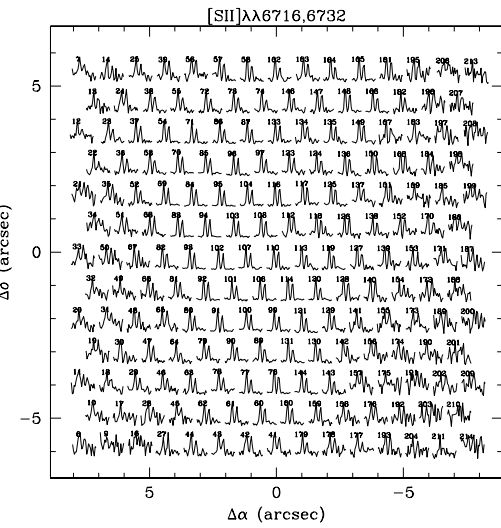


Fig. 14.— Two-dimensional distribution of $[\text{S II}]\lambda\lambda 6716, 6731$ (6720–6785 Å).